Series of molecular-like doubly excited states of a quasi-three-body Coulomb system

M. Génévriez* and M. Jungers
Institute of Condensed Matter and Nanosciences,
Université catholique de Louvain, BE-1348 Louvain-la-Neuve, Belgium

C. Rosen and U. Eichmann†
Max-Born-Institute, 12489 Berlin, Germany
(Dated: September 25, 2025)

We investigated resonant multiphoton excitation of high-angular-momentum doubly excited states of the strontium atom, a quasi-three-body Coulomb system, both experimentally and theoretically. A series of highly doubly excited states converging to the double ionization threshold was identified and reproduced by first-principles calculations, which provided access to the two-electron wavefunctions of the resonances. In these states, the outer electron is dynamically localized at large distances by pendulum-like oscillations of the inner electron across the nucleus. A complementary simple molecular-like adiabatic model offers a clear interpretation of the correlated two-electron motion and suggests that the series is a general feature of highly doubly excited states of atoms and molecules.

Two highly excited electrons moving in the Coulomb field of a doubly charged nucleus form a strongly correlated quantum system with a fascinatingly rich spectrum of resonances [1, 2]. As a prototype of the three-body Coulomb problem, it stimulated intense experimental and theoretical work that revealed the existence of longer-lived resonances in a two-electron phase space that is otherwise largely chaotic [3]. In such states the two electrons can follow remarkably correlated orbits [4–6], such as the frozen-planet orbit, in which the two electrons are dynamically localized on the same side of the nucleus at specific orbit radii, the collinear eZe orbit, or the Langmuir orbit [1, 7, 8].

Doubly-excited resonances have been experimentally detected as sharp lines in photoexcitation spectra [5, 9–11] and, with the advent of ultrafast lasers, their dynamics were unraveled in the time domain [12–14]. To date, experimentally identified series belong to those converging to a single ionization threshold: one electron remains near the nucleus while the other explores increasingly distant orbits, giving rise to a Rydberg-like progression of asymmetric states [15–18]. In contrast, series converging to the double ionization threshold remain unexplored experimentally despite abundant theoretical work [1, 7, 8]. These series mark a distinct, fascinating regime in which the independent-electron picture looses its meaning entirely and all three Coulomb interactions play an integral part in the correlated electron-pair dynamics [1].

In helium, series converging to the double ionization threshold have escaped observation due to the small transition dipole moment from the ground state and the excitation energies in the far ultraviolet range [17–19]. Alkaline-earth atoms such as strontium offer a more favorable platform because multiphoton resonant excitation makes it possible to prepare doubly excited states inaccessible by one-photon excitation from the ground state [5, 20] with high-resolution table-top lasers [5, 20–23]. Their two valence electrons, together with the doubly charged ion core, form quasi-three-body Coulomb systems [2] that have been crucial to investigate planetary states [16, 24], i.e., asymmetric doubly excited states for which the approximate individual principal quantum numbers of the two electrons are different ($N < n$). Recent theoretical effort [6, 11, 25] has also made possible to describe very high lying doubly-excited states of alkaline-earth atoms, well beyond the degree of excitation reached in earlier pioneering work [26].

In this letter we report the experimental observation of a series of doubly excited states converging to the double-ionization threshold. The series is supported by a remarkable, correlated two-electron orbit which differs from those theoretically identified in previous works: The inner electron oscillates between opposite sides of the nucleus while the outer electron is confined in a molecular-like potential at large distances. We thus propose to refer to these states as pendular-planet states (PPS). The states are identified in high-resolution spectra of doubly excited Sr that we recorded and their assignment is supported by accurate calculations from first principles. The PPS orbits are then identified using the wavefunctions extracted from our calculations and the origin of the series is explained using a simple adiabtic molecular-like model, which provides a clear physical picture of this unsual series.

In the experiment, doubly excited states of Sr are prepared below the $Sr^+(N = 9 - 17)$ ionization thresholds following the well established sequential resonant multiphoton excitation scheme [16, 27–29] shown in Fig. 1. Note that the independent-particle quantum numbers adopted for the states classification are only approximate because of the high degree of electronic correlation. Briefly, Sr atoms in an effusive beam are first excited from the $5s^2$ ground state via an intermediate resonance to $5sn_il_i$ Rydberg state ($n_i = 18$, $l_i = 15$)

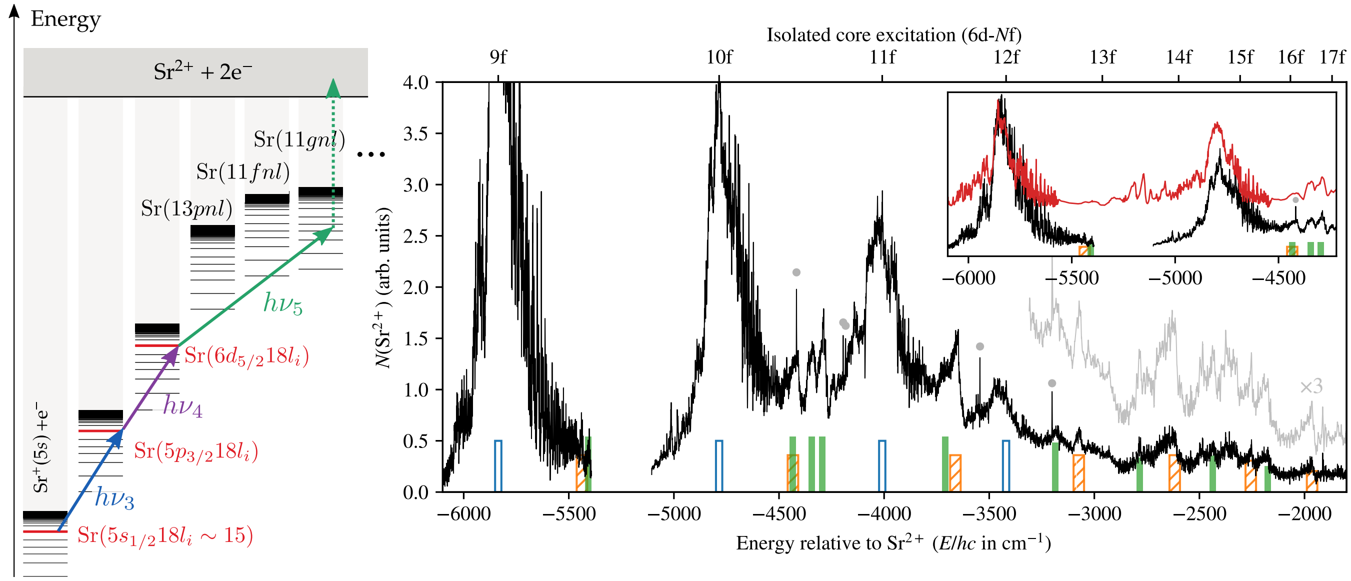

FIG. 1. (Left) Resonant multiphoton excitation scheme. (Right) Experimental spectrum in the region of the $\mathrm{Sr}^+(N = 9 - 17)$ ionization thresholds. The wavenumber scale is given relative to the Sr^{2+} double ionization threshold to facilitate analysis. The gray line shows the spectrum above -3800 cm^{-1} scaled by 3 for visibility. The energies of the $\mathrm{Sr}^+(6dnl - Nfnl)$ transitions are shown in the upper horizontal scale. The lines centered around those transitions and visible in the spectrum are marked by vertical unfilled blue bars. The series of lines under investigation is marked by the filled green bars. Hatched orange bars denote a different series (see text). Spurious sharp resonances in the Sr^+ ion are marked by the full gray circles. The inset shows a comparison between the experimental spectrum (lower full black line) and the theoretical spectrum (upper full red line) in the $N = 9 - 10$ region.

using two pulsed dye lasers and a “Stark switching” electric field [30, 31] (see End Matter for details). After a time delay of about 2 μs to adiabatically switch the Stark field to zero, another two pulsed dye lasers excite the atoms to the $6d_{5/2}18l_i$ state via the intermediate $5p_{3/2}18l_i$ state. Finally, a fifth pulsed dye laser is scanned to excite the atoms further to doubly excited states near the $\mathrm{Sr}^+(N = 9 - 17)$ thresholds. Approximately 200 ns after the fifth laser pulse, a large electric field (~ 12 kV/cm) is applied. It field ionizes atoms in high lying doubly excited states and the highly excited Sr^+ ions produced upon autoionization or upon photoionization by the fifth laser pulse [11, 28]. Sr^{2+} ions are recorded as a function of the wavenumber of the fifth laser.

The experimental spectrum, shown in Fig. 1, exhibits series of lines with a rich substructure that are superimposed, at higher photon energies, onto a continuum. The most prominent features, marked by unfilled blue bars, are centered around the $\mathrm{Sr}^+(6d - Nf)$ dipole-allowed transitions of the isolated ion. Similar isolated-core-excitation (ICE) lines have been investigated at a lower threshold ($N = 7$) [32], and the detailed analysis of the present ones will be given elsewhere. Above $-3250\ \mathrm{cm}^{-1}$ the ICE series vanishes but the spectrum is not structureless and two series of lines remain visible. The first series, marked by the hatched orange bars, is associated to high lying Rydberg-like states located below each hydrogenic ionization threshold $\mathrm{Sr}^+(N, L > 3)$. Its analysis is ongoing. The second set of resonances, marked by the filled green bars, is the PPS series investigated in the present paper. It is remarkable because it remains visible even for very high excitation ($N = 16$) and because it converges to the double ionization threshold but does *not* follow the Rydberg formula or any other formulas describing the energies of series of doubly-excited states (see [1] for a review).

To identify the nature of the PPS series we ran extensive theoretical calculations using the method of configuration interaction with exterior complex scaling (CI-ECS) [25]. It treats the two-electron motion from first principles while accounting for the effect of the Sr^{2+} closed-shell ion core with an accurate model potential. CI-ECS is capable of describing highly doubly excited states of alkaline-earth atoms [6, 11, 22, 33], a challenging task as the correlated motion of the two electrons must be treated over large radial distances ($> 1000\, a_0$), the density of states increases rapidly ($10^6\ \mathrm{eV}^{-1}$) and many decay channels are open. The calculations reported here correspond to a degree of excitation ($N \sim 9 - 10$) that is well beyond what had been previously calculated for any species other than helium ($N = 6$) [6, 26]. Calculations details are given in the end matter.

To assess the accuracy of the calculations, the photoionization spectrum calculated with CI-ECS (see [6] for details) is compared to the experimental spectrum in

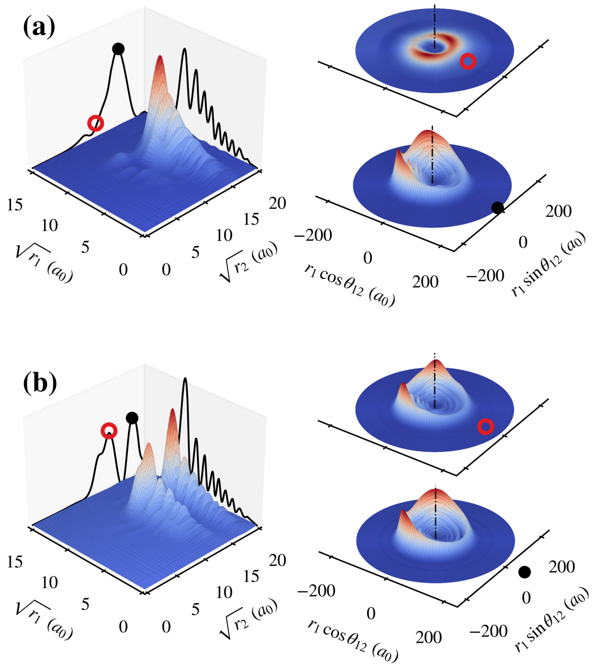

FIG. 2. Two-dimensional representations of the two-electron probability density for states associated to the leftmost (a) and central (b) PPS resonances near -4500 cm^{-1} (see text). The left panels correspond to the densities integrated over all spatial coordinates but r_1 and r_2. Projections onto the r_1 and r_2 axes are also shown. The right panels show the conditional density when the outer electron is fixed at a given radius, shown by the full black or red circles also shown on the left panels.

the inset of Fig. 1. To take into account the small populations of states with $l_i \neq 15$ in the experiment (see end matter), the theoretical spectra were calculated for several values of l_i $(10-18)$ and subsequently added to reproduce as well as possible the experimental data. The agreement between theory and experimental is excellent over the entire wavenumber range and makes us confident that the theoretical calculations capture all relevant details of the electron dynamics.

CI-ECS reveals that only a handful of resonances contribute to the PPS lines in the experimental spectrum, typically one per value of the total orbital-angular-momentum and spin quantum numbers. The analysis of the CI coefficients further reveals that these states have predominant $Ndnl$ character, with $l = 14$ for the resonance near -5500 cm^{-1} and $l = 16$ for those near -4500 cm^{-1}. Their autoionization lifetimes fall in the range from 100 fs to a few picoseconds.

Two-electron dynamics are revealed by inspecting the two-electron probability density $|\Psi(\boldsymbol{r}_1, \boldsymbol{r}_2)|^2$ along the radial coordinates r_1 and r_2 after integrating over all other spatial dimensions. They are shown in Fig. 2 (left column) for the the two leftmost resonances near -4500 cm^{-1} with a total-angular-momentum quantum number of $L = 17$. Note that the functions do not include antisymmetrization for clarity. Antisymmetrized densities are obtained by mirror symmetry about the $r_1 = r_2$ axis.

The densities in the left column of Fig. 2 do not show a strong dependency of the radial motion of one electron on the other. The inner-electron density has 8 minima along r_1, a value compatible with the predominant $12d$ character of the inner-electron wavefunction deduced from CI-ECS [34]. The outer-electron density of the leftmost state [Fig. 2(a)], on the other hand, shows no clear minima. If electron correlations were neglected, this would be surprising as the wavefunction of a highly excited electron has many nodes. The absence of nodes thus suggests that the electronic repulsion plays an essential role and, together with the Coulomb attraction of the Sr^{2+} core and the centrifugal barrier, gives rise to a local dynamical potential-energy well in which the outer electron evolves. The state in Fig. 2(a) may be associated to the ground state of that potential, while the state associated with the second resonance [Fig. 2(b)], with one node, is the first excited state. The departure of the wavefunctions of Fig. 2 from what would be expected if electron correlations were small, as in the case of planetary series observed in earlier experiments, highlights the fundamentally different nature of the PPS series.

Correlations in the angular motion of the two electrons are best observed by fixing the outer electron at a given radius r and plotting the conditional density $|\Psi(r_1, \theta_{12}|r_2 = r)|^2$ (right panels in Fig. 2), integrated over all other spatial dimensions. θ_{12} is the angle between the two electrons. When the outer electron is near its most probable position, angular correlations are strong and the two electrons reside predominantly on opposite sides of the nucleus. As the outer electron gets closer to the nucleus [Fig. 2(a), top right graph], angular correlations drastically change, a fact to which we shall come back later. Similar observations can be made about the probability densities of other members of the PPS series and an example is shown in the end matter.

CI-ECS calculations successfully reproduce the PPS resonances observed in the experiment and predict the two-electron dynamics, but do not give an intuitive picture as to their physical origin. To do so we turn to a simple model in which the fast motion of the inner electron is adiabatically decoupled from the one of the (comparatively slower) outer electron. This is akin to a Born-Oppenheimer approximation [32, 35] in which r_2 would be the internuclear distance (see End Matter for details). The outer electron generates an electric field which we assume to be uniform in the region where the inner electron evolves and of strength $-1/r_2^2$ in atomic units. Because of that field the inner electron undergoes a Stark shift that depends on r_2, and we write its energy as $E_1^{\alpha,|\Lambda|}(-1/r_2^2)$. Λ is the projection of $\boldsymbol{L}$ onto the adiabtic axis $\boldsymbol{r}_2$, and α denotes all other quantum numbers required to label the inner-electron Stark state. The inner-electron Stark energies are depicted in Fig. 3(a) as a function of the electric-field strength. Within these approximations, the outer electron evolves in an adiabatic potential $V(r_2)$ that is the sum of the screened Coulomb attraction of the core $(-1/r_2)$, the centrifugal barrier $(l_2(l_2+1)/2r_2^2)$, and the dynamically-Stark-shifted energy $E_1^{\alpha,|\Lambda|}$ of the inner electron,

$$V(r_2) = -\frac{1}{r_2} + \frac{l_2(l_2+1)}{2r_2^2} + E_1^{\alpha,|\Lambda|}(-1/r_2^2). \qquad (1)$$

For the calculations shown below we take $l_2 = 16$ and $|\Lambda| = 1$ based on the analysis of the CI coefficients and wavefunctions given above.

Whereas the screened Coulomb attraction and the centrifugal barrier are monotonous with r_2, the Stark energies $E_1^{\alpha,|\Lambda|}$ are not due to avoided crossings between states [see Fig. 3(a)]. As a result the adiabatic potentials $V(r_2)$, shown in Fig. 3(b), may exhibit local extrema. A local minimum is clearly visible for those potentials for which the inner electron is predominantly in the $Sr^+(Nd)$ state at large distances (dashed gray lines). It arises from the avoided crossings shown by the red shaded areas in Fig. 3(a), which involve the Stark states associated, at zero field, to the $Sr^+(Nd)$ state and the uppermost state from the $Sr^+(N-2L)$ hydrogenic manifold. Remarkably, the lowest levels of the potential wells (purple lines) match the energies of the PPS resonances (filled green bars, right panel) within less than 1%. For these calculation the small avoided crossings in the repulsive part of the potentials were assumed to be traversed diabatically.

The model also explains why the PPS resonances are well visible in the spectra. At the minimum of the potential wells the inner-electron state has a strong Nf character $c_{Nf}(r_2)$ [see colorscale in Fig. 3(b)]. The transition electric-dipole moment from the $6dn_il_i$ initial state is thus large when the outer electron is near the bottom of the well. It is the case for low-lying states but, as the degree of excitation of the outer electron increases, the wavefunctions spread out and the transition moment decreases. This is illustrated by the horizontal black bars in Fig. 3(b), whose lengths are proportional to the effective, scaled transition moment $\int_0^\infty \mathrm{d}r_2 \psi_2^*(r_2) c_{Nf}(r_2) d_{6d-Nf} N^{3/2} \psi_{n_il_i}(r_2)$, with d_{6d-Nf} the transition dipole moment of the isolated ion and $\psi_{n_il_i}(r_2)$ and $\psi_2(r_2)$ the radial wavefunctions of the outer electron in the initial and final states, respectively.

The correlated two-electron motion encoded in the densities of Fig. 2 is also in agreement with, and clarified by, the model. The most probable radius for the outer electron in the ground state of the potential near -4500 cm^{-1} is $r_2^{\max} = 243\ a_0$, in excellent agreement with the one extracted from CI-ECS [237 a_0, Fig. 2(a)]. In both calculations the outer-electron density has no nodes while the first excited state shows one node at

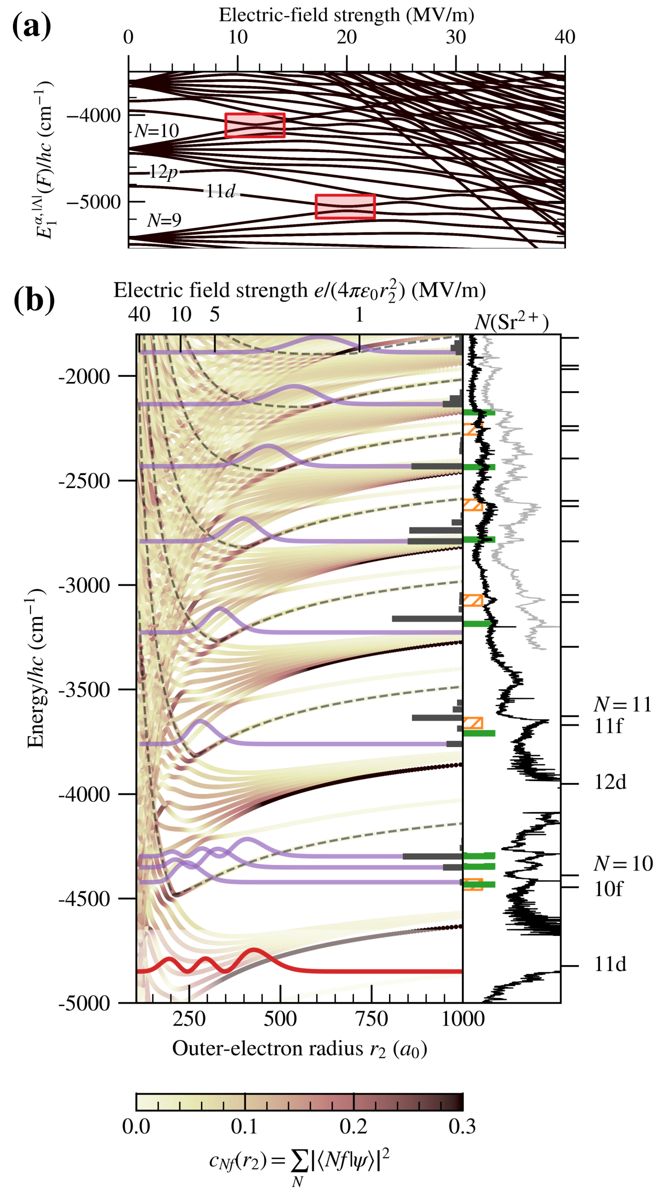

FIG. 3. (a) Stark energies of Sr^+ in the $N = 9-11$ region. (b) Adiabatic potentials $V(r_2)$. The colorscale shows the Nf character of the inner-electron wavefunction. The radial probability densities $|\psi(r_2)|^2$ of the outer electron in the $6d18l_i$ state and in low-lying states of the potentials shown by the dashed lines are displayed as the red and purple lines, respectively. The horizontal black bars show the energy levels of the dashed-line potentials and their lengths give the transition strengths from the initial state. The right panel shows the experimental spectrum as in Fig. 1.

$r_2 \sim 250\ a_0$ [Fig. 2(b)]. For sufficiently large r_2 the inner-electron wavefunction has a predominant Nd character and 8 nodes, as expected. In the repulsive part of the potential, the dominant Nd character is however lost and the inner-electron acquires some character associated to the uppermost states of the $(N-2)$ Stark manifold [Fig. 3(a)]. In such states the electron localizes on the side of the nucleus given by the direction of the electric field [36] and the same effect is observed in the two-electron density of Fig. 2(a). For a small r_2 value (red circle), the inner electron is indeed predominantly on the same side of the nucleus as the outer electron. The two-electron motion can thus be semi-classically interpreted as follows: as the the outer electron oscillates in its potential well the dipole moment of the "inner electron + ion core" system undergoes a periodic pendulum-like motion such that, when r_2 is small, it effectively prevents the outer electron from penetrating into the inner region. From the lifetime of the state ($\tau \sim 300$ fs) and the spacing between adjacent energy levels in the well (~ 100 cm^{-1}) we deduce that the inner electron undergoes about 6 such flip-flops before the system spontaneously decays by autoionization.

Conclusions - We have identified a series of molecular-like doubly excited states of a quasi three-body Coulomb system converging to the double ionization both theoretically and experimentally. The states, which we call pendular-planet states because of the underlying two-electron motion, find their physical origins in avoided crossings between Stark states, a phenomenon that occurs in all systems except hydrogen-like atoms. For this reason, we expect the series to be a general feature of the doubly excited states of atoms and molecules. Remarkably, a similar mechanism is responsible for the long-range molecular binding between an ion and a Rydberg atom [37–39]. In the latter case the electric field is generated by an ion in the vicinity of the Rydberg atom whereas, in the present case, the electric field is the one of the outer electron that surrounds the Sr^+ ion, itself in a Rydberg state. Both cases illustrate that the quasi-three-body Coulomb problem possesses series of resonances that, because its third body is not so well defined [40], are different from the exact counterpart. Observing and characterizing the states discussed above in other atomic and molecular systems is an exciting perspective for future work that could be facilitated, in particular in more complex systems, by the use of the simple model and physical picture we developed.

This work was supported by the Fonds de la Recherche Scientifique under MIS Grant No. F.4027.24 and IISN Grant No. 4.4504.10. Computational resources were provided by the supercomputing facilities of the Université catholique de Louvain (CISM/UCL) and the Consortium des Équipements de Calcul Intensif en Fédération Wallonie Bruxelles (CÉCI) funded by the Fond de la Recherche Scientifique de Belgique (F.R.S.-FNRS) under convention 2.5020.11 and by the Walloon Region.

* matthieu.genevriez@uclouvain.be
† eichmann@mbi-berlin.de

[1] G. Tanner, K. Richter, and J. M. Rost, Rev. Mod. Phys. **72**, 497 (2000).
[2] M. Aymar, C. H. Greene, and E. Luc-Koenig, Rev. Mod. Phys. **68**, 1015 (1996).
[3] K. Richter, G. Tanner, and D. Wintgen, Phys. Rev. A **48**, 4182 (1993).
[4] K. Richter and D. Wintgen, Phys. Rev. Lett. **65**, 1965 (1990).
[5] U. Eichmann, V. Lange, and W. Sandner, Phys. Rev. Lett. **64**, 274 (1990).
[6] M. Génévriez, C. Rosen, and U. Eichmann, Phys. Rev. A **104**, 012812 (2021).
[7] K. Richter and D. Wintgen, J. Phys. B: At. Mol. Opt. Phys. **24**, L565 (1991).
[8] J. Müller and J. Burgdörfer, Phys. Rev. Lett. **70**, 2375 (1993).
[9] M. Domke, C. Xue, A. Puschmann, T. Mandel, E. Hudson, D. A. Shirley, G. Kaindl, C. H. Greene, H. R. Sadeghpour, and H. Petersen, Phys. Rev. Lett. **66**, 1306 (1991).
[10] A. Czasch, M. Schöffler, M. Hattass, S. Schössler, T. Jahnke, Th. Weber, A. Staudte, J. Titze, C. Wimmer, S. Kammer, M. Weckenbrock, S. Voss, R. E. Grisenti, O. Jagutzki, L. Ph. H. Schmidt, H. Schmidt-Böcking, R. Dörner, J. M. Rost, T. Schneider, C.-N. Liu, I. Bray, A. S. Kheifets, and K. Bartschat, Phys. Rev. Lett. **95**, 243003 (2005).
[11] M. Génévriez and U. Eichmann, Phys. Rev. A **107**, 012817 (2023).
[12] S. N. Pisharody and R. R. Jones, Science **303**, 813 (2004).
[13] C. Ott, A. Kaldun, L. Argenti, P. Raith, K. Meyer, M. Laux, Y. Zhang, A. Blättermann, S. Hagstotz, T. Ding, R. Heck, J. Madroñero, F. Martín, and T. Pfeifer, Nature **516**, 374 (2014).
[14] A. Kaldun, A. Blättermann, V. Stooß, S. Donsa, H. Wei, R. Pazourek, S. Nagele, C. Ott, C. D. Lin, J. Burgdörfer, and T. Pfeifer, Science **354**, 738 (2016).
[15] P. Camus, S. Cohen, L. Pruvost, and A. Bolovinos, Phys. Rev. A **48**, R9 (1993).
[16] U. Eichmann, V. Lange, and W. Sandner, Phys. Rev. Lett. **68**, 21 (1992).
[17] K. Schulz, G. Kaindl, M. Domke, J. D. Bozek, P. A. Heimann, A. S. Schlachter, and J. M. Rost, Phys. Rev. Lett. **77**, 3086 (1996).
[18] Y. H. Jiang, R. Püttner, R. Hentges, J. Viefhaus, M. Poygin, C. Cacho, U. Becker, J. M. Rost, and G. Kaindl, J. Phys. B: At. Mol. Opt. Phys. **39**, L9 (2005).
[19] Y. H. Jiang, R. Püttner, D. Delande, M. Martins, and G. Kaindl, Phys. Rev. A **78**, 021401 (2008).
[20] P. Camus, T. F. Gallagher, J. M. Lecomte, P. Pillet, L. Pruvost, and J. Boulmer, Phys. Rev. Lett. **62**, 2365 (1989).
[21] M. Génévriez, D. Wehrli, J. Agner, and F. Merkt, Int. J. Mass Spectrom. **435**, 209 (2019).
[22] M. Génévriez, D. Wehrli, and F. Merkt, Phys. Rev. A **100**, 032517 (2019).
[23] R. C. Teixeira, A. Larrouy, A. Muni, L. Lachaud, J.-M. Raimond, S. Gleyzes, and M. Brune, Phys. Rev. Lett. **125**, 263001 (2020).
[24] I. C. Percival, Proc. R. Soc. Lond. A **353**, 289 (1977).
[25] M. Génévriez, Mol. Phys. **119**, e1861353 (2021).
[26] R. P. Wood and C. H. Greene, Phys. Rev. A **49**, 1029 (1994).
[27] U. Eichmann, P. Brockmann, V. Lange, and W. Sandner,

J. Phys. B: At. Mol. Opt. Phys. **22**, L361 (1989).
[28] C. Rosen, M. Dörr, U. Eichmann, and W. Sandner, Phys. Rev. Lett. **83**, 4514 (1999).
[29] U. Eichmann, T. F. Gallagher, and R. M. Konik, Phys. Rev. Lett. **90**, 233004 (2003).
[30] W. E. Cooke, T. F. Gallagher, S. A. Edelstein, and R. M. Hill, Phys. Rev. Lett. **40**, 178 (1978).
[31] R. R. Jones and T. F. Gallagher, Phys. Rev. A **42**, 2655 (1990).
[32] K. D. Heber, M. Seng, M. Halka, U. Eichmann, and W. Sandner, Phys. Rev. A **56**, 1255 (1997).
[33] D. Wehrli, M. Génévriez, and F. Merkt, Phys. Rev. A **100**, 012515 (2019).
[34] The quantum defect of the Sr^+ Nd series is ~ 1.5.
[35] J. M. Feagin and J. S. Briggs, Phys. Rev. A **37**, 4599 (1988).
[36] T. F. Gallagher, *Rydberg Atoms* (Cambridge University Press, Cambridge, 1994).
[37] M. Deiß, S. Haze, and J. Hecker Denschlag, Atoms **9**, 34 (2021).
[38] A. Duspayev, X. Han, M. A. Viray, L. Ma, J. Zhao, and G. Raithel, Phys. Rev. Research **3**, 023114 (2021).
[39] N. Zuber, V. S. V. Anasuri, M. Berngruber, Y.-Q. Zou, F. Meinert, R. Löw, and T. Pfau, Nature **605**, 453 (2022).
[40] K. Codling, Nature **344**, 194 (1990).
[41] T. N. Rescigno and C. W. McCurdy, Phys. Rev. A **62**, 032706 (2000).
[42] C. A. Nicolaides and D. R. Beck, Phys. Lett. A **65**, 2 (1978).
[43] B. Simon, Phys. Lett. A **71**, 211 (1979).
[44] B. Grémaud and P. Gaspard, J. Phys. B: At. Mol. Opt. Phys. **31**, 1671 (1998).
[45] J. W. Warner, L. S. Bartell, and S. M. Blinder, Int. J. Quantum Chem. **18**, 921 (1980).
[46] V. Lange, M. A. Khan, U. Eichmann, and W. Sandner, Z Phys D - Atoms, Molecules and Clusters **18**, 319 (1991).
[47] P. A. Braun, V. N. Ostrovsky, and N. V. Prudov, Phys. Rev. A **42**, 6537 (1990).
[48] K. Richter, J. S. Briggs, D. Wintgen, and E. A. Solov'ev, J. Phys. B: At. Mol. Opt. Phys. **25**, 3929 (1992).
[49] T. P. Grozdanov, A. A. Gusev, E. A. Solov'ev, and S. I. Vinitsky, Eur. Phys. J. D **74**, 161 (2020).

End matter

Experimental details

Stark switching. In the experiment, $5sn_il_i$ Rydberg states with large orbital angular momenta ($l_i \sim 15$) are produced by the "Stark switching" technique [30, 31]. Two pulsed dye lasers pumped by an excimer laser first excite Sr atoms in their $5s^2$ ground state via an intermediate resonance to a $5sn_ik_i$ Rydberg Stark state in the presence of a static electric field. The field is then slowly turned off ($\sim 2\mu$s) such that the Stark state adiabtically evolves into a $5sn_il_i$ Rydberg state, the value of l_i being determined by the value of k_i. In the present case we choose $l_i = 15$. Nonadiabatic effects as the field is switched off and stray electric fields in the chamber can cause the transfer of a small part of the population to other, neighbouring l values [6, 15].

Sr^{2+} production. During the 5-photon excitation to highly doubly excited states, the pulse energies of the first four lasers are kept low (~ 10 μJ) and the fifth laser pulse is more intense (~ 1 mJ). The latter is intense enough to photoionize the high lying doubly excited states, leaving Sr^+ in high Rydberg states [28]. Autoionization of the doubly excited states can also produce highly excited Sr^+ ions. The $\sim$ 12-kV/cm electric field pulse, applied 200 ns after the fifth laser pulse, field ionizes the highly excited Sr^+ ions and doubly-exicted Sr atoms produced by the lasers, yielding the Sr^{2+} ions detected in the experiment.

Configuration interaction with exterior complex scaling

The method of configuration interaction with exterior complex scaling (CI-ECS) [25] aims at accurately describing highly doubly excited states of alkaline-earth atoms [6, 11, 22, 33]. It treats the motion of the two highly excited electrons of Sr explicitely while the influence of the electrons of the Sr^{2+} closed-shell core is accounted for with an empirical model potential $V_l(r)$ [2, 25], yielding the following two-electron Hamiltonian

$$H = -\frac{1}{2}\boldsymbol{\nabla}_1^2 - \frac{1}{2}\boldsymbol{\nabla}_2^2 + V_{l_1}(r_1) + V_{l_2}(r_2) + V_{l_1 l_2}(\boldsymbol{r}_1, \boldsymbol{r}_2) + \frac{1}{r_{12}}. \tag{2}$$

$\boldsymbol{r}_1$ and $\boldsymbol{r}_2$ are the coordinates of the electrons with respect to the nucleus and $r_{12} = |\boldsymbol{r}_1 - \boldsymbol{r}_2|$. The potentials $V_l(r)$ include monoelectronic core-polarization terms while the term $V_{l_1 l_2}(\boldsymbol{r}_1, \boldsymbol{r}_2)$ accounts for dielectronic core polarization [25]. The latter is included for completeness only as its influence on the energies of the states presented above is negligible compared to experimental resolution (~ 1 cm^{-1}). The potentials $V_l(r)$ yield energies of Sr^+ accurate to better than a few cm^{-1} [6, 22].

The two-electron Schrödinger equation is solved using a basis of antisymmetrized products of one-electron spin-orbitals whose radial parts are numerical functions obtained with a finite-element discrete-variable-representation technique [41]. We use exterior complex scaling [42, 43] to treat resonances and continuum processes with square integrable functions, i.e., to be able to carry out the calculations in a box of finite size ($1420\,a_0$). In the present calculations, 80 000 two-electron basis functions are used. The outer electron is described with a large set of spin-orbitals, including in particular accurate Rydberg states up to $n = 25$. The basis set describing the inner electron is truncated to all states up to the $Sr^+(N = 12)$ hydrogenic manifold. Angular momenta are LS coupled and the spin-orbit interaction is neglected because both electrons are highly excited and thus predominantly far from the nucleus. The large, complex-symmetric Hamiltonian matrix built from the two-electron functions is diagonalized in the energy range of interest with a complex-symmetric Lanczos algorithm, yielding the complex-scaled wavefunctions and energies of bound states, resonances and continuum states. We have checked that the resonances energies and widths below the $N = 11$ threshold are converged to better than a few cm^{-1} with respect to the basis set size, complex-scaling radius and angle.

Electron dynamics are visualized as in Fig. 2 starting from the wavefunctions $\Psi(\boldsymbol{r}_1, \boldsymbol{r}_2)$ calculated with CI-ECS. To reduce the number of dimensions we integrate over the three Euler angles that define the orientation of the electron–electron–Sr^{2+}-ion plane in space [6, 44] to obtain the reduced two-electron probability density

$$\rho(r_1, r_2, \cos\theta_{12}) = \langle \Psi | \delta(r_1 - r_1')\delta(r_2 - r_2')\delta(\cos\theta_{12} - \cos\theta_{12}') | \Psi \rangle\,, \tag{3}$$

where $\delta(x)$ are Dirac delta functions. $\delta(\cos\theta_{12} - \cos\theta_{12}')$ is expanded in terms of Legendre polynomials [45] to evaluate the matrix element. ρ depends only on the two electronic radial distances r_1 and r_2 and the interelectronic angle θ_{12}, and can be readily used to generate the densities shown in Fig. 2.

Calculations at a higher threshold

The size of the full CI-ECS basis set increases very rapidly close to the double-ionization threshold, making converged calculations for $Sr^+(N > 10)$ computationally too heavy. The analysis carried out in the main text however suggests that, to compute the resonances under consideration, it is sufficient to consider inner-electron states associated to the $Sr^+(N-2)$ and $Sr^+(N-1)$ hydrogenic manifold, and all states in between with nonzero quantum defects. Such an ensemble is indeed sufficient to reproduce the avoided crossing responsible for the potential well and the strong Nf character at its bottom.

To verify this we ran a CI-ECS calculation in which the set of basis functions describing the inner electron is limited to all states between, and including, the $N = 12$ and $N = 13$ manifolds. The truncation of the basis set means that most decay channels are neglected, and that the calculation is not fully converged. We do not expect to reach quantitative agreement with experiment but aim at providing a qualitative confirmation that the essential two-electron dynamics are well described by the truncated basis. The calculated photoionization spectrum is compared to the experimental one in Fig. 4(b). The resonance marked by the filled green bar is indeed well reproduced by the theoretical calculation and the underlying resonance wavefunctions [Fig. 4(a)], similar to those of Fig. 2, confirm the attribution to the series described in the main text.

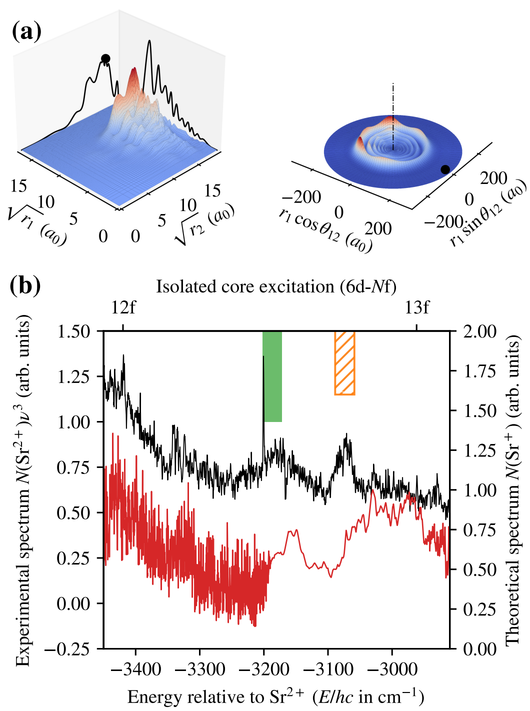

FIG. 4. (a) Same as Fig. 2 for the resonance at -3200 cm^{-1} [filled green bar in panel (b)] with a total-orbital-angular-momentum quantum number $L = 13$. (b) Experimental (red) and theoretical (black) spectra in the region of the $\mathrm{Sr}^+(N = 12-13)$ ionization thresholds. Figure details are the same as those of Fig. 1 (right panel).

Adiabatic model potential

The adiabatic potential (1) is obtained from the two-electron Hamiltonian (2), neglecting dielectronic core polarization, in two steps. First, we assume that the motion of the two electrons can be adiabatically separated,

$$\Psi(\boldsymbol{r}_1, \boldsymbol{r}_2) = \psi(\boldsymbol{r}_1; r_2)\phi(\boldsymbol{r}_2), \tag{4}$$

with the wavefunction $\psi(\boldsymbol{r}_1; r_2)$ describing the motion of the faster inner electron depending parametrically on the radial position r_2 of the slower one – much as in the Born-Oppenheimer approximation where the electronic wavefunction of a diatomic molecule parametrically depends on the internuclear distance. The function ψ statisfies the equation

$$\left(-\frac{1}{2}\boldsymbol{\nabla}_1^2 + V_{l_1}(r_1) + \frac{1}{r_{12}}\right)\psi = \epsilon(r_2)\psi. \tag{5}$$

The multipole expansion of the electronic repulsion reads

$$\frac{1}{r_{12}} = \sum_q \frac{r_<^q}{r_>^{q+1}} P_q(\cos\theta_{12}), \tag{6}$$

with $r_<$ ($r_>$) being the smallest (largest) of the two radial distances r_1 and r_2, respectively, and P_q is the Legendre polynomial of order q. Keeping only the monopole and dipole terms ($q = 0$ and 1) and assuming that $r_2 > r_1$, a property easily verified by inspecting the probability densities in Fig. 2, we obtain

$$\left(-\frac{1}{2}\boldsymbol{\nabla}_1^2 + V_{l_1}(r_1) + \frac{1}{r_2} + \frac{z_1}{r_2^2}\right)\psi = \epsilon(r_2)\psi, \tag{7}$$

with $z_1 = r_1\cos\theta_{12}$ the projection of $\boldsymbol{r}_1$ onto the adiabatic axis $\boldsymbol{r}_2$. Eq. (7) describes the valence electron of the Sr^+ ion in the presence of an electric field of strength $1/r_2^2$ applied along the z direction, and an additional constant energy offset $1/r_2$. Its eigenvalues are therefore

$$\epsilon(r_2) = E_1^{\alpha,|\Lambda|}(r_2) + \frac{1}{r_2}, \tag{8}$$

with $E_1^{\alpha,|\Lambda|}(r_2)$ the energies of the Stark states of the Sr^+ ion (Fig. 3). Finally, we assume that, because the angular momentum of the outer electron is large, it does not penetrate much in the Sr^{2+} core region and $V_{l_2}(r_2)$ is well approximated by the pure Coulomb potential $-2/r_2$. This approximation is justified by the fact that the quantum defects of the high-l states of Sr^+ are very small [46]. The radial, adiabatic, one-electron Schrödinger equation for the *outer* electron can now be written as

$$\left(-\frac{1}{2}\frac{\mathrm{d}^2}{\mathrm{d}r_2^2} - \frac{1}{r_2} + \frac{l_2(l_2+1)}{2r_2^2} + E_1^{|\Lambda|}(r_2)\right)\phi(r_2) = E\psi(r_2), \tag{9}$$

which justifies the potential for the outer electron given in Eq. (1).

More quantitative adiabatic and nonadiabtic potentials for the outer electron have been developped [47–49]. The present one is simple and qualitative – we do not expect the adiabatic approximation to hold as well as it does in molecules – but provides a remarkably clear physical insight into the origin of the PPS and the electronic dynamics at play.